THE JOURNAL OF PHYSICAL CHEMISTRY C

Article

pubs.acs.org/JPCC

Structurally Accurate Model for the "29"-Structure of Cu_xO/Cu(111): A DFT and STM Study

Andrew J. Therrien,[†] Renqin Zhang,[‡] Felicia R. Lucci,[†] Matthew D. Marcinkowski,[†] Alyssa Hensley,[‡] Jean-Sabin McEwen,[*,‡,§,∥] and E. Charles H. Sykes[*,†]

[†]Department of Chemistry, Tufts University, Medford, Massachusetts 02155, United States

[‡]The Gene and Linda Voiland School of Chemical Engineering and Bioengineering, Washington State University, Pullman, Washington 99164, United States

[§]Department of Physics and Astronomy, Washington State University, Pullman, Washington 99164, United States

[∥]Department of Chemistry, Washington State University, Pullman, Washington 99164, United States

Supporting Information

ABSTRACT: Copper is a common catalyst for many important chemical reactions including low-temperature water gas shift, selective catalytic reduction of NO_x, methanol synthesis, methanol steam reforming, and partial oxidation of methanol. The degree of surface oxidation, or the oxidation state of the active site, during these reactions has been debated and is known to have a large influence on the reaction rates. Therefore, elucidating the atomic-scale structure of copper surface oxides is an important step toward a fuller understanding of reaction mechanisms in heterogeneous catalysis. The so-called "29" monolayer oxide film is a common intermediate in the oxidation of Cu(111). The large size of its unit cell has thus far prevented the development of a definitive model for its structure. Using high-resolution scanning tunneling microscopy (STM) and density functional theory (DFT) calculations, we arrive at a model for the "29" Cu_xO film on Cu(111). There is very good agreement between experimental and computational STM images over a range of biases. Through the construction of a phase diagram from first-principles, we further find that the "29" structure derived from the DFT calculations is indeed the most stable structure under the experimental conditions considered. This work yields an accurate picture of the atomic scale structure of the "29" oxide film and therefore a basis for beginning to understand adsorption sites and reaction mechanisms on this catalytically relevant surface.

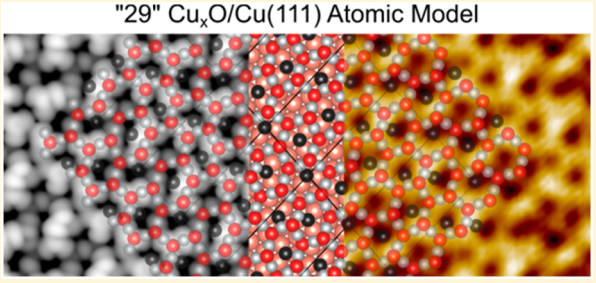

INTRODUCTION

Copper-based catalysts are used in many heterogeneous catalytic processes such as low-temperature water gas shift,[1,2] CO oxidation,[3−7] methanol synthesis,[8−11] methanol steam reforming,[12] the partial oxidation of methanol to formaldehyde,[13−15] and the epoxidation of hydrocarbons.[16,17] Cu can also be exchanged within a zeolite with a chabazite structure, which is the current state-of-the-art catalyst in the selective catalytic reduction of NO_x to ammonia.[18] The oxidation state of Cu plays a crucial role in these reactions and has been the subject of much debate.[19] Partially oxidized Cu has been shown to be a very good catalyst for many of these processes,[8,19−23] as pure metallic Cu cannot survive under redox conditions,[24] making the details of such surface structures important to understand. There is also a large amount of evidence that the oxidation state of the Cu can cycle between Cu^{1+} and Cu^{2+} throughout the catalytic cycle for the selective catalytic reduction of NO_x with ammonia when a Cu-exchanged zeolite is used as the catalyst.[25] Furthermore, Cu_2O has been extensively studied due to its photovoltaic and photocatalytic properties.[26−29]

The oxidation of Cu has been thoroughly investigated to understand these catalytically relevant surfaces and gain a fundamental understanding of the bulk oxidation process.[30,31] At low temperatures (∼100 K) a molecularly bound peroxo species forms on the Cu surface, but at room temperature O_2 readily dissociates.[32] At low O surface coverages on Cu(111), O adatoms preferentially sit in fcc 3-fold hollow sites.[33,34] As the O coverage is increased disordered oxide structures are formed, which grow from step edges and have been shown to refacet to expose [100] type steps.[34−37] At higher substrate temperatures ordered Cu_2O-like films form on Cu(111). Rodriguez and coworkers have reported the formation of honeycomb oxide phases, which can also exhibit 5−7 defects and O vacancies.[6,7,38,39] When the surface layer is saturated with O_2 at ∼423 or ∼673 K, the "44" or "29" oxide structures are formed, respectively, and are referred to as such because their unit cell areas are 44 and 29 times larger than the underlying

Received: February 5, 2016
Revised: April 11, 2016
Published: April 22, 2016

DOI: 10.1021/acs.jpcc.6b01284
J. Phys. Chem. C 2016, 120, 10879−10886

Cu(111) unit cell.[37,40−42] The "29" oxide has a slightly higher O coverage than the "44" oxide. Finally, a Cu_2O(100)-like oxide phase has been discovered using a hyperthermal molecular beam,[43−45] which relaxes to the "29" structure after annealing to 620 K.[46] These structures are precursors to bulk Cu_2O growth, which begins to take place at high oxygen exposures, typically >10^6 Langmuirs (1 Langmuir = 1 × 10^{-6} Torr s).[47]

Of these known copper oxide reconstructions, structural models for only the honeycomb and corresponding defective oxides[6,38,48,49] and the Cu_2O(100)-like structure[50] have been theoretically calculated and experimentally verified. In regard to the heavily studied "44" and "29" oxides, a variety of surface science techniques have been used to show that these structures are Cu_2O(111)-like films that have been distorted to be commensurate with the underlying Cu(111) substrate.[30,31] Bowker and coworkers proposed structural models based on scanning tunneling microscopy (STM) studies,[37] but the models have yet to be verified; hence there are no well-accepted models for these oxides. The perfect Cu_2O(111) surface is made up of fused hexagonal rings with a periodicity of 0.6 nm and occupying a 0.316 nm^2 area.[40] The rings are made up of linear O−Cu−O bonds, which buckle, resulting in raised and depressed O atoms;[40,51,52] however, when grown on Cu(111) this oxide film must distort to be commensurate with the Cu(111) substrate and take on the symmetry of the "44" or "29" oxide. The most stable conformations of the "44" and "29" structures are thought to involve eight and six of these hexagonal rings per oxide unit cell, respectively.[37] In other density functional theory (DFT) studies, simpler models with similar O coverages have been used in place of the "44" and "29" structures,[48,53−56] as the "44" and "29" oxides are very computationally expensive to model due to their large size and complexity. This simpler model is constructed by building a Cu_2O-like layer on top Cu(111) with a $p(4 \times 4)$ supercell containing nine Cu ions and seven O ions.[48,53,55] The calculated area per hexagonal ring in this model is 0.315 nm^2, whereas the area per ring in the "44" and "29" oxides is 0.314 and 0.276 nm^2, respectively. Therefore, it is somewhat reasonable to use this structure to simulate the "44" oxide due to their similar hexagonal ring densities; however, this model ignores the distortion of Cu_xO layer in the "29"structure and has a very different oxide ring density, making a better model for the "29" structure needed. In this study we propose a full structural model for the "29" oxide model using experimental data from high-resolution STM, DFT calculations, and simulated STM images.

EXPERIMENTAL AND COMPUTATIONAL METHODS

Scanning Tunneling Microscopy. The oxide film was prepared in a ultrahigh vacuum chamber ($P = 2 \times 10^{-10}$ mbar) where the Cu(111) surface was cleaned by Ar^+ sputtering and annealing to 1000 K. As illustrated in Figure 1, the "29" oxide film was formed by holding the Cu(111) crystal at 650 ± 20 K and exposure to O_2 gas (Airgas, USP grade) at a pressure of 5 × 10^{-6} mbar for 3 min. The sample was then transferred to the STM chamber ($P = 1 \times 10^{-11}$ mbar) into the precooled STM stage. Imaging was conducted using a Low-Temperature Omicron NanoTechnology STM at 80 K.

Density Functional Theory. DFT calculations were performed with the Vienna Ab initio Simulation Package (VASP) code.[57,58] The projector-augmented wave (PAW)[59,60] method and the generalized-gradient approximation (GGA), using the PBE[61] functional, were employed for the treatment of the electron−ion interactions and the exchange-correlation effects, respectively. With its PAW potentials, VASP combines the accuracy of all-electron methods with the computational efficiency of plane-wave approaches. For the ionic relaxation, the conjugate-gradient algorithm was applied. The electronic wave functions were expanded in a basis set of plane waves with kinetic-energy cutoffs of 500 eV. The "29" Cu_xO/Cu(111) surfaces were modeled by putting one layer of Cu_xO on the Cu(111) surface with a $\sqrt{13}R46.1° \times 7R21.8°$ supercell that was four layers thick. The bottom two layers of the slab were kept fixed in their bulk positions at a lattice constant of 3.635 Å, which is consistent with the reported computational value of 3.634 Å[6] and the experimental value of 3.62 Å.[62] Detailed information on the "29" structure of Cu(111) surface can be found in Figures S1 and S2 of the Supporting Information. The Cu_xO layer is made from fused hexagonal rings, each with six Cu atoms and six O atoms. There are six of these hexagonal rings per "29" oxide unit cell, which has 18 Cu atoms and 12 O atoms in the Cu_xO layer. There are also O adatoms in the center of the rings, which adsorb at either fcc or hcp hollow sites of the Cu(111) surface (see Figure S2 of the Supporting Information), where they are bound most strongly.[33] Table 1 lists the possible total number of O adatoms and the corresponding O coverage of the "29" Cu_xO/Cu(111) structure. The vacuum thickness was ∼12 Å. The unit cells were sampled with (1 × 2 × 1) Monkhorst−Pack k-point grids. A Methfessel−Paxton smearing of 0.2 eV was used to improve the convergence, and the total energy was extrapolated to zero

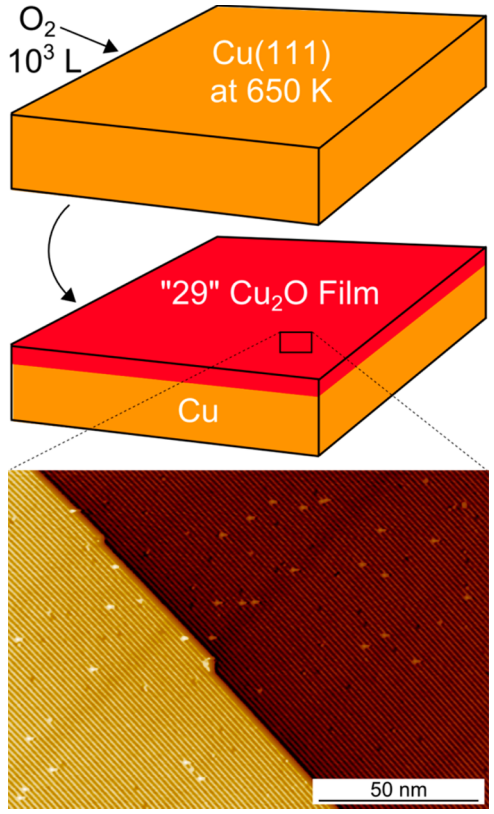

Figure 1. Schematic depicting the sample preparation for the "29" oxide. A representative STM image reveals an ordered domain that runs for many hundreds of nanometers; scanning conditions 0.9 V, 0.1 nA.

DOI: 10.1021/acs.jpcc.6b01284
J. Phys. Chem. C 2016, 120, 10879−10886

Table 1. Possible Number of O Adatoms per "29" Oxide Unit Cell and the Corresponding Surface Coverage with Respect to Cu(111)[a]

surface structure	O coverage (ML)	E_f (eV)
Cu(111)	0	0.00
N = 0	0.414	−1.99
N = 1	0.448	−1.96
N = 2	0.483	−1.92
N = 3	0.517	−1.91
N = 4	0.552	−1.88
N = 5	0.586	−1.91
N = 6	0.621	−1.84
Cu_2O(111)	0.535	−1.43

[a]In the right-hand column, the average formation energy per O atom, E_f, is reported.

Kelvin. The total energy convergence threshold was set to 10^{-6} eV and the geometries were considered to be fully relaxed when the forces were <0.02 eV/Å. The computational STM images were generated by using the constant current model, which is implemented in the p4vasp program using the Tersoff−Hamann approach.[63,64] In addition, the calculated lattice constant of bulk Cu_2O is 4.312 Å. The Cu_2O(111) surface is modeled by using a $p(2 \times 2)$ supercell, which has size of 12.196 × 12.196 Å.

RESULTS AND DISCUSSION

As shown in Figure 1, the "29" Cu_xO oxide film was prepared by exposing a clean Cu(111) crystal held at 650 ± 20 K to ∼1000 L of O_2. The wide-scale STM image at the bottom of Figure 1 shows the characteristic row-like structure of the oxide overlayer. Because of the fact that these rows are rotated from the high-symmetry directions of the underlying Cu(111) lattice, there are six possible orientations of the "29" structure, as previously shown by low-energy electron diffraction (LEED);[37] however, in the area shown in Figure 1, only one domain of the "29" oxide is present, evidencing its long-range order. Atomic size defects, currently of unknown identity, can be seen as bright and dark spots in the image; however, these defects are present at very low concentrations, with a surface coverage of only ∼0.02% of a monolayer, with respect to Cu(111), counted over a total area >70 000 nm^2.

As previously mentioned, it has been shown by a number of techniques that the "29" oxide is similar to the Cu_2O(111) surface structure.[30] The most stable conformation is thought to involve six of these hexagonal rings per "29" oxide unit cell, which is also true of the structural model proposed by Bowker and coworkers.[37] The outstanding questions are the exact geometry of these rings and if there are additional O adatoms in the structure. Using nuclear reaction analysis (NRA), Besenbacher and coworkers experimentally measured the O coverage of the "29" oxide to be 0.52 ± 0.05 ML (1 ML is defined as the Cu(111) packing density of 1.776×10^{15} atoms cm^{-2}).[41] This measurement also showed that the "29" oxide has saturated the surface layer of Cu with O but does not form bulk Cu_2O. Presented in Table 1 is the corresponding O coverage for each possible number of added O atoms per "29" oxide unit cell. From this point forward, N will be used to represent the number of O adatoms in a given "29" oxide model.

The average formation energy, E_f, per oxygen atom of each "29" Cu_xO/Cu(111) candidate is also presented in Table 1. E_f can be calculated by

$$E_f = \frac{1}{y}\left(E_{total} - E_{clean} - xE_{bulk}^{Cu} - \frac{y}{2}E_{O_2}\right) \quad (1)$$

where E_{total} is the total energy of the "29" oxide candidate and E_{clean} is the total energy of a clean Cu(111) slab. Variables x and y are the number of Cu and O atoms in the Cu_xO layer, including the O adatoms, respectively. Finally, E_{bulk}^{Cu} and E_{O_2} are the total energies of a bulk Cu atom and an O_2 molecule in the gas phase, respectively. Table 1 lists the average formation energy per oxygen atom of the N = 0−6 structures. In general, O adsorption is exothermic, resulting in the negative values for E_f. It is found that E_f of the Cu_xO layers change only slightly for N = 0−6 and are all near −1.9 eV. Therefore, the average stability of each O atom of the Cu_xO layer is almost independent of the total number of O adatoms. The average formation energy of the Cu_2O(111) surface is also listed in Table 1 for comparison. It is found that the average formation energy per oxygen atom is less favorable in the case of Cu_2O(111) than for any of the "29" Cu_xO/Cu(111) candidates, indicating that it is harder and requires a higher O chemical potential to form bulk Cu_2O than the "29"

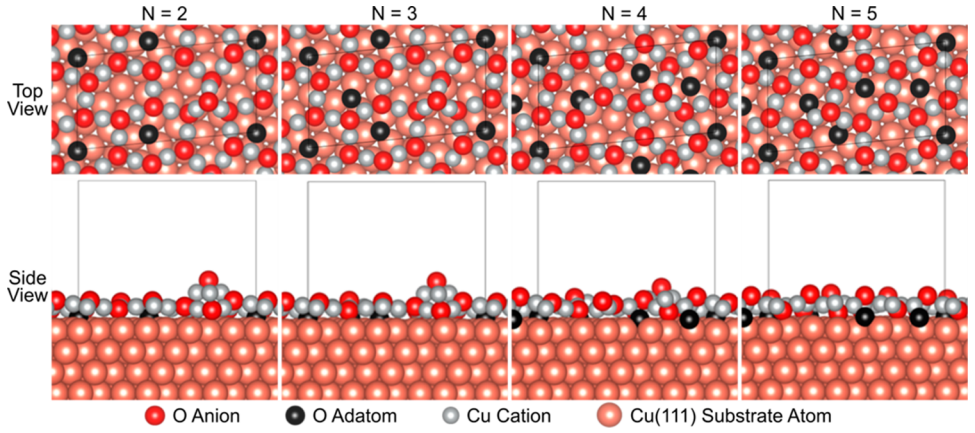

Figure 2. Top and side views of the candidates of the "29" oxide structure. The lowest energy DFT calculated "29" oxide structural models for N = 2, 3, 4, and 5 O adatoms per unit cell are presented. The red balls and gray balls represent the O anion and Cu cation in the Cu_xO layer, respectively. The black and cupreous spheres represent O adatoms and Cu atoms in Cu(111) substrate, respectively.

DOI: 10.1021/acs.jpcc.6b01284
J. Phys. Chem. C 2016, 120, 10879−10886

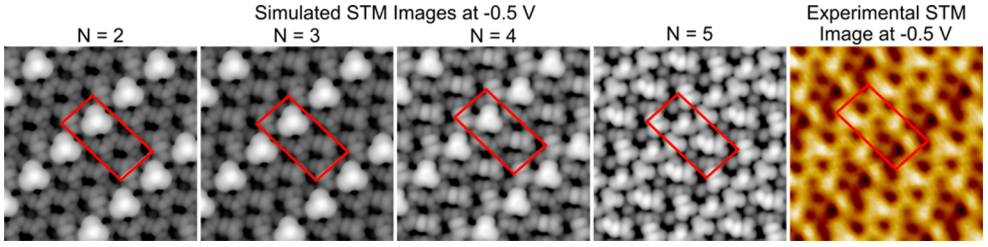

Figure 3. Simulated STM images at −0.5 V sample bias of the structural models presented in Figure 2 alongside an experimental STM image at the same scanning bias. The contrast in the images is a convolution of the relative changes in topography and conductance. The "29" oxide unit cell is highlighted by the red parallelogram. All images are 4 × 4 nm^2.

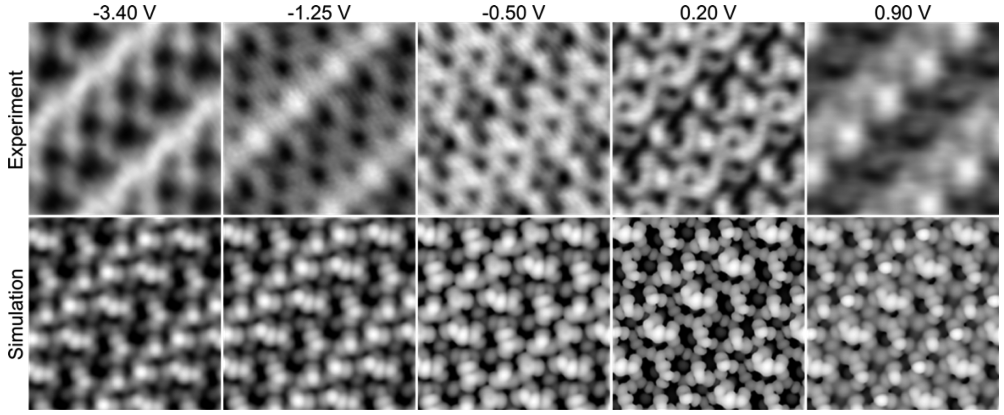

Figure 4. Experimental STM images of the "29" oxide (top row) and simulated STM images of the N = 5 structure (bottom row). At different scanning biases the surface appears very different by STM, which is also captured by the simulated STM images, showing excellent agreement between experiment and theory. All images are 3.5 × 3.5 nm^2.

structure, which is consistent with the experimental observation that the "29" oxide preludes bulk Cu_2O formation.

Some structural candidates for the "29" structure can be discarded by comparing the surface O coverages listed in Table 1 to the experimentally determined O coverage of 0.52 ± 0.05 ML. For N = 6 the corresponding O coverage is significantly greater than that of the experimentally determined value. Likewise, N = 0 and 1 have O coverages much lower than 0.52 ± 0.05 ML; therefore, both can be discarded as a candidates for the "29" oxide structure.[41] Shown in Figure 2 are the structures of the remaining candidates for the "29" oxide, namely, N = 2−5. In each case there are many possible permutations, or configurations, of the placement of O adatoms in the hexagonal rings. Each permutation of O adatoms was calculated, with the restriction of one O adatom per ring and maintaining the integrity of each hexagonal ring, and the most stable structures are presented in Figure 2. Some of the less favorable configurations can be found in the Supporting Information. With the most stable configurations representing each possible number of O adatoms, N, a general trend becomes evident that as the surface becomes more oxidized the overall structure of the film becomes flatter. In the cases of N = 2 and 3, a large protrusion is formed in oxide overlayer. The height of corrugation can be clearly seen from the side views displayed in Figure 2. The resulting height variations of the N = 2 and 3 Cu_xO layers are 2.963 and 2.848 Å, respectively, measured from the vertical position of lowest to the highest point in the oxide layer. In the cases of N = 4 and 5, the height variations are 2.431 and 1.705 Å, respectively; significantly less that the height variations of N = 2 and 3.

In Figure 3 the simulated STM image at a sample bias of −0.5 V is displayed for each of the "29" oxide candidates, and the image on the far right is an experimental STM image of the "29" oxide film. STM images are a convolution of topographic and electronic information, in which relative height and conductance are represented by the brightness of a feature. As seen for the N = 2 and 3 structures, the formation of the large protrusion in the Cu_xO layer results in a large bright feature in the simulated STM image. Although, to a lesser extent, the N = 4 structure also generates an appreciably large bright feature. The N = 5 structure, on the contrary, is relatively flat with the pores of the hexagonal rings appearing as the lowest points in the simulated STM image and the buckling of the rings responsible for the corrugation. With regard to the experimental STM image, there is no feature with such a dramatic height difference from the rest of the surface as seen in the simulated N = 2, 3, and 4 structures. This leaves the N = 5 structure as the most consistent model with the experimental STM data.

As evident in Figure 3, the simulated STM images are much sharper than the experimental STM images. This is due to the fact that the resolution of experimental STM is limited by experimental noise and the shape of the STM tip; however, simulated STM does not have such limitations and the resulting image is a representation of the calculated spatial electron density integrated from the Fermi level to the scanning bias, but most importantly, the agreement between the N = 5 simulated STM image and the experimental STM image in Figure 3 is in the symmetry and the location of surface features. This is easily identified by referencing the unit cell highlighted by the red parallelogram; the positions of the local maxima and minima within the unit cells match incredibly well.

To further verify that the N = 5 structure is an accurate model for the "29" oxide, simulated STM images at different

DOI: 10.1021/acs.jpcc.6b01284
J. Phys. Chem. C 2016, 120, 10879−10886

voltages were compared with experimental STM images, which can be seen in Figure 4. It can be seen experimentally that the appearance of the oxide changes significantly as the imaging bias is adjusted, which is due to changes in the local density of states available for tunneling into or out of. These changes are captured very well by the simulated STM images. The images are displayed in a way that each image is superimposable with any other image in Figure 4. This is made clear by certain features that can be recognized between a number of experimental images. Most easily identifiable are the brightest features in the 0.9 V experimental image, in which bright circular units are arranged in-line diagonally from the bottom left to the top right of the image. These discrete bright features can be found in the same position in the other STM images. To compare the experimental to the simulated STM images, let us begin with the −3.4 and −1.25 V experimental images. In both cases, bright rows can be seen running diagonally across the surface with dark circular depressions filling the space between the bright rows. The simulated STM images also show this, with the bright rows and dark depressions appearing in the same relative locations. Moving to the −0.5 and 0.2 V STM images, there is no longer the appearance of these bright rows and the surface appears to be much more porous, which is echoed in the simulated STM images. Finally, in the 0.9 V experimental STM image, the area above of the discrete bright features previously mentioned is bright, while below the bright features it is darker. This is very well echoed in the simulated STM image in which there are bright features decorating the upper side of the discrete bright protrusions and dark depressions on the lower side. The agreement between the simulated and experimental STM images through all the complex changes induced by adjusting the scanning bias is very compelling, further supporting the fact that the $N = 5$ structure is in fact an atomically accurate model for the complex "29" oxide film.

Another piece of evidence in support of the accuracy of the $N = 5$ model for the "29" oxide structure is shown in Figure 5, in which a simulated STM image, the $N = 5$ atomic model, and an experimental STM image at −0.5 V are shown together. In the simulated STM image it is shown how the atomic model overlays with the image. In this way, it is clear how the model overlays with the experimental STM image. The dark features in the image are the pores of the hexagonal rings which is consistent with the pores of the rings being topographically lower than the rest of the surface. Interestingly, the hexagonal ring without an O adatom does not appear significantly different from any of the other rings that include an O adatom. Our structure appears to be more corrugated and buckled than the previous model for the "29" oxide proposed by Bowker and coworkers.[37]

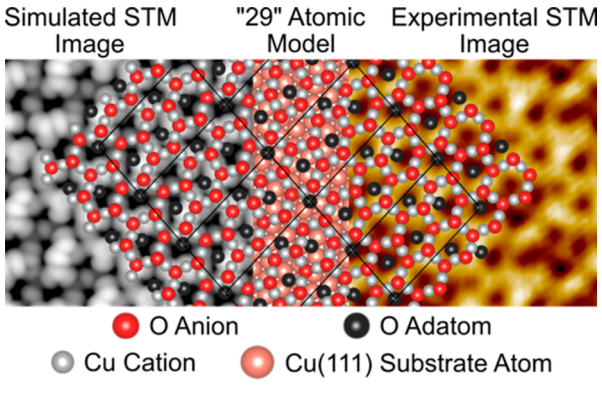

Figure 5. From left to right, a simulated STM image at −0.5 V of the $N = 5$ structure, the atomic model for $N = 5$, and an experimental STM image at −0.5 V. It can be clearly seen how the structural model of the "29" oxide overlays very well with the experimental STM image. Images are 3.5 × 3.5 nm^2.

Another difference between the models is that the bright features in the reported STM image by Bowker and coworkers were assumed to result from an increase in conductance due to O vacancies, or a lack of O adatoms.[37] This was a reasonable conclusion, as the opposite is true in which isolated O adatoms on Cu(111) are known to appear as depressions due to a depletion of the density of states around the Fermi level.[34] O vacancies resulting in bright features by STM have been reported in more reduced Cu_xO/Cu(111) films, specifically the "O-deficient" phase;[6] however, in this highly oxidized and tightly packed "29" structure, the hexagonal ring without an O adatom appears in STM images very similarly to those rings with an O adatom at the tested scanning biases.

Finally, it is worthwhile to study the stability of the "29" Cu_xO/Cu(111) under different oxidation conditions. The surface energy of formation for Cu oxide species can be calculated by

$$\gamma_f = \frac{1}{A}(E_{total} - E_{clean} - x\mu_{Cu} - y\mu_O) \quad (2)$$

where E_{total} is the total energy of Cu oxide species and E_{clean} is the total energy of a clean Cu(111) slab. Variables x and y are the number of Cu and O atoms in the Cu_xO layer, respectively. A is the area of the oxide surface. The oxygen chemical potential μ_O can be related to the total energy of an isolated O_2 molecule as reference zero, where $\mu_O = \Delta\mu_O + \frac{1}{2}E_{O_2}$. The Cu chemical potential can be approximated by using the total energy of bulk Cu, E^{Cu}_{bulk}.[55] Therefore, eq 2 can be written as

$$\gamma_f = \frac{1}{A}\left(E_{total} - E_{clean} - xE^{Cu}_{bulk} - \frac{y}{2}E_{O_2} - y\Delta\mu_O\right) \quad (3)$$

The oxygen chemical potential can be related to the temperature, T, and the O_2 partial pressure, p^{O_2}, via the ideal gas formulas. Detailed information can be found in the Supporting Information. We remark that the oxygen chemical potential could also be related to the pressure of other molecules at a certain temperature, such as CO and CO_2. In addition, we estimated the error in the GGA approximation by increasing the cutoff energy from 500 to 600 eV. The error is found to be ∼0.02 eV. For a particular oxygen chemical potential, the error of 0.02 eV can be translated to an O_2 pressure error of $\sim 0.06p^{O_2}$, or 6% error, in the temperature range of 650 ± 20 K that was studied.

Shown in Figure 6a is a phase diagram of a handful of experimentally observed oxide phases of Cu. These are, in increasing degree of oxidation, clean Cu(111), O/Cu(111) at a coverage of 1/16 ML, the honeycomb oxide,[6] the "29"structure with $N = 5$, and Cu_2O(111). The detailed information on the O/Cu(111), honeycomb oxide, and Cu_2O(111) can be found in the Supporting Information. Most importantly, the phase diagram reveals that under very low O chemical potentials isolated O adatoms on Cu(111) at a coverage of 1/16 ML are the most favorable structure. As the O chemical potential is increased, the honeycomb oxide becomes favorable over a small range of O chemical potentials until eventually the "29"

DOI: 10.1021/acs.jpcc.6b01284
J. Phys. Chem. C 2016, 120, 10879−10886

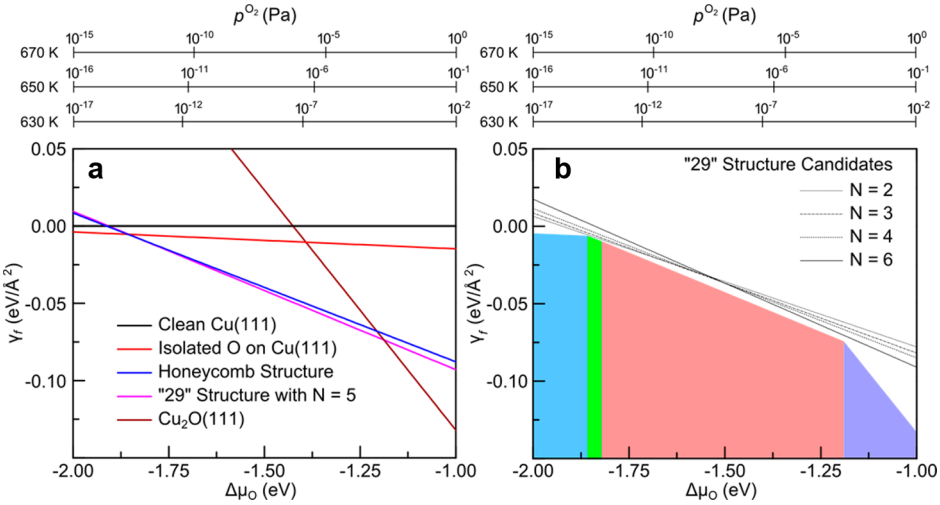

Figure 6. Phase diagram as a function of $\Delta\mu_O$ of (a) clean Cu(111), isolated O adatoms on Cu(111), "29" oxide with $N = 5$, $Cu_2O(111)$ surface, and the honeycomb structure. (b) Other "29" oxide structures with $N = 2$, 3, 4, and 6. The blue, green, red, and purple areas represent the most favorable structure of O adatoms on Cu(111), the honeycomb structure, "29" structure with $N = 5$, and $Cu_2O(111)$, respectively. The corresponding pressure of O_2 under different temperatures is also given.

structure presented above ($N = 5$) becomes the most favorable. It is reasonable that the honeycomb oxide and the "29" oxide are very similar energetically, as both are surface $Cu_2O(111)$-like structures; only the "29" is more compressed, resulting in a greater surface O density. Finally, when the O chemical potential is high enough, bulk oxidation takes place and $Cu_2O(111)$ is the preferred species. Shown above the phase diagrams in Figure 6 are the corresponding O_2 partial pressures, p^{O_2}, at different temperatures. The phase diagram is also in excellent agreement with previous experimental studies in regard to the O_2 exposure required to obtain isolated O adatoms, the honeycomb oxide, the "29" structure, and bulk Cu_2O.[6,30,31,37] If the "29" structure, or a similar surface oxide, is present under catalytic reaction conditions, it will interact strongly with CO and CO_2, therefore making them potential active sites for reactions involving such molecules. Figure 6b shows the phase diagram of the other previously discussed "29" structure candidates, namely, $N = 2$, 3, 4, and 6. The colored regions displayed in Figure 6b represent the conditions in which other structures from Figure 6a are the most stable. In the light-blue region, the isolated O adatoms are favored, in the green region the honeycomb oxide, in the red region the $N = 5$ structure, and in the purple region $Cu_2O(111)$ is favored. As further evidence that $N = 5$ is the accurate "29" structure, Figure 6b shows that under no conditions are the $N = 2$, 3, 4, or 6 structures the preferred species.

The "29" oxide acts as a precursor to bulk oxidation, as it is the surface-saturated O/Cu(111) phase. The "29" structure is highly strained, evidenced by a greater surface O concentration than bulk $Cu_2O(111)$, as shown in Table 1. This strain is displayed by the compression of the $Cu_2O(111)$ surface unit cell by 16%, giving rise to the buckling of the hexagonal rings in the "29" model. Upon additional oxidation, further strain is avoided by O dissolution into the bulk resulting in Cu_2O formation.[41] Importantly, Figure 6 shows that the "29" structure is stable over a range of O pressures in which neither pure metallic Cu nor bulk Cu_2O is stable, making this structure catalytically relevant for many processes.

CONCLUSIONS

There are numerous industrially important processes that use Cu-based catalysts, many of which are believed to occur on partially oxidized Cu surfaces, meaning the oxidation state of Cu is neither purely metallic nor purely cuprous. Of the known handful of Cu_2O-like surface oxides, the surface O-saturated structure, referred to as the "29" structure, has gone unsolved due to its large size and complexity. In this study an atomically accurate model for the "29" structure is proposed that shows excellent agreement between DFT-simulated STM images and experimental STM images over a range of scanning biases. This structure is composed of six hexagonal rings per unit cell, five of which host an O adatom. The "29" oxide has a higher surface O concentration than bulk $Cu_2O(111)$ and is shown to be the preferred structure under moderate oxidation conditions, preluding bulk Cu_2O formation. With this atomically precise model of the "29" structure, adsorption sites and reaction mechanisms on this catalytically relevant surface can now be probed in greater detail.

ASSOCIATED CONTENT

Supporting Information

The Supporting Information is available free of charge on the ACS Publications website at DOI: 10.1021/acs.jpcc.6b01284.

Report of the possible configurations for the "29" oxide structure for $N = 4$ and 5. Also included is an explanation of the phase diagram chemical potential calculations and a report of the other structures in the phase diagram, specifically, the isolated O on Cu(111), the honeycomb structure, and $Cu_2O(111)$. (PDF)

AUTHOR INFORMATION

Corresponding Authors

*J.-S.M.: Tel: 509-335-8580. E-mail: js.mcewen@wsu.edu.
*E.C.H.S.: Tel: 617-627-3773. Email: Charles.Sykes@tufts.edu.

Notes

The authors declare no competing financial interest.

DOI: 10.1021/acs.jpcc.6b01284
J. Phys. Chem. C 2016, 120, 10879−10886

■ ACKNOWLEDGMENTS

Financial support was provided by the National Science Foundation EAGER program under contract no. CBET-1552320. The work at Tufts was supported by the Department of Energy BES under grant no. DE-FG02-05ER15730. M.M. thanks Tufts Chemistry for an Illumina Fellowship. It was also partially funded by USDA/NIFA through Hatch Project #WNP00807 titled: "Fundamental and Applied Chemical and Biological Catalysts to Minimize Climate Change, Create a Sustainable Energy Future, and Provide a Safer Food Supply". A portion of the computer time for the computational work was performed using EMSL, a national scientific user facility sponsored by the Department of Energy's Office of Biological and Environmental Research and located at PNNL. PNNL is a multi-program national laboratory operated for the U.S. DOE by Battelle.

■ REFERENCES

(1) Newsome, D. S. The Water-Gas Shift Reaction. *Catal. Rev.: Sci. Eng.* **1980**, *21*, 275−318.
(2) Ovesen, C. V.; Stoltze, P.; Nørskov, J. K.; Campbell, C. T. A Kinetic Model of the Water Gas Shift Reaction. *J. Catal.* **1992**, *134*, 445−468.
(3) Eren, B.; Lichtenstein, L.; Wu, C. H.; Bluhm, H.; Somorjai, G. A.; Salmeron, M. Reaction of CO with Preadsorbed Oxygen on Low-Index Copper Surfaces: An Ambient Pressure X-Ray Photoelectron Spectroscopy and Scanning Tunneling Microscopy Study. *J. Phys. Chem. C* **2015**, *119*, 14669−14674.
(4) Domagala, M. E.; Campbell, C. T. The Mechanism of CO Oxidation Over Cu(110): Effect of CO Gas Energy. *Catal. Lett.* **1991**, *9*, 65−70.
(5) Szanyi, J.; Goodman, D. W. CO Oxidation on a Cu (100) Catalyst. *Catal. Lett.* **1993**, *21*, 165−174.
(6) Yang, F.; Choi, Y.; Liu, P.; Hrbek, J.; Rodriguez, J. A. Autocatalytic Reduction of a Cu_2O/Cu(111) Surface by CO: STM, XPS, and DFT Studies. *J. Phys. Chem. C* **2010**, *114*, 17042−17050.
(7) Baber, A. E.; Xu, F.; Dvorak, F.; Mudiyanselage, K.; Soldemo, M.; Weissenrieder, J.; Senanayake, S. D.; Sadowski, J. T.; Rodriguez, J. A.; Matolín, V.; et al. In Situ Imaging of Cu_2O Under Reducing Conditions: Formation of Metallic Fronts by Mass Transfer. *J. Am. Chem. Soc.* **2013**, *135*, 16781−16784.
(8) Klier, K. Methanol Synthesis. *Adv. Catal.* **1982**, *31*, 243−313.
(9) Chinchen, G. C.; Waugh, K. C.; Whan, D. A. The Activity and State of the Copper Surface in Methanol Synthesis Catalysts. *Appl. Catal.* **1986**, *25*, 101−107.
(10) Szanyi, J.; Goodman, D. W. Methanol Synthesis on a Cu(100) Catalyst. *Catal. Lett.* **1991**, *10*, 383−390.
(11) Behrens, M.; Studt, F.; Kasatkin, I.; Kühl, S.; Hävecker, M.; Abild-Pedersen, F.; Zander, S.; Girgsdies, F.; Kurr, P.; Kniep, B.-L.; et al. The Active Site of Methanol Synthesis over Cu/ZnO/Al_2O_3 Industrial Catalysts. *Science* **2012**, *336*, 893−897.
(12) Palo, D. R.; Dagle, R. A.; Holladay, J. D. Methanol Steam Reforming for Hydrogen Production. *Chem. Rev.* **2007**, *107*, 3992−4021.
(13) Russell, J. N.; Gates, S. M.; Yates, J. T. Reaction of Methanol with Cu(111) and Cu(111) + O(ads). *Surf. Sci.* **1985**, *163*, 516−549.
(14) Boucher, M. B.; Marcinkowski, M. D.; Liriano, M. L.; Murphy, C. J.; Lewis, E. A.; Jewell, A. D.; Mattera, M. F. G.; Kyriakou, G.; Flytzani-Stephanopoulos, M.; Sykes, E. C. H. Molecular-Scale Perspective of Water-Catalyzed Methanol Dehydrogenation to Formaldehyde. *ACS Nano* **2013**, *7*, 6181−6187.
(15) Bluhm, H.; Havecker, M.; Knop-Gericke, A.; Kleimenov, E.; Schlogl, R.; Teschner, D.; Bukhtiyarov, V. I.; Ogletree, D. F.; Salmeron, M. Methanol Oxidation on a Copper Catalyst Investigated Using in Situ X-Ray Photoelectron Spectroscopy. *J. Phys. Chem. B* **2004**, *108*, 14340−14347.
(16) Cropley, R. L.; Williams, F. J.; Urquhart, A. J.; Vaughan, O. P. H.; Tikhov, M. S.; Lambert, R. M. Efficient Epoxidation of a Terminal Alkene Containing Allylic Hydrogen Atoms: Trans-Methylstyrene on Cu{111}. *J. Am. Chem. Soc.* **2005**, *127*, 6069−6076.
(17) Duzenli, D.; Seker, E.; Senkan, S.; Onal, I. Epoxidation of Propene by High-Throughput Screening Method over Combinatorially Prepared Cu Catalysts Supported on High and Low Surface Area Silica. *Catal. Lett.* **2012**, *142*, 1234−1243.
(18) Kwak, J. H.; Tonkyn, R. G.; Kim, D. H.; Szanyi, J.; Peden, C. H. F. Excellent Activity and Selectivity of Cu-SSZ-13 in the Selective Catalytic Reduction of NO_x with NH_3. *J. Catal.* **2010**, *275*, 187−190.
(19) Grabow, L. C.; Mavrikakis, M. Mechanism of Methanol Synthesis on Cu through CO_2 and CO Hydrogenation. *ACS Catal.* **2011**, *1*, 365−384.
(20) Kanai, Y.; Watanabe, T.; Fujitani, T.; Uchijima, T.; Nakamura, J. The Synergy Between Cu and ZnO in Methanol Synthesis Catalysts. *Catal. Lett.* **1996**, *38*, 157−163.
(21) Huang, T.; Tsai, D. CO Oxidation Behavior of Copper and Copper Oxides. *Catal. Lett.* **2003**, *87*, 173−178.
(22) Torres, D.; Lopez, N.; Illas, F.; Lambert, R. M. Low-Basicity Oxygen Atoms: A Key in the Search for Propylene Epoxidation Catalysts. *Angew. Chem.* **2007**, *119*, 2101−2104.
(23) Jernigan, G. G.; Somorjai, G. A. Carbon Monoxide Oxidation over Three Different Oxidation States of Copper: Metallic Copper, Copper (I) Oxide, an Copper (II) Oxide-A Surface Science and Kinetic Study. *J. Catal.* **1994**, *147*, 567−577.
(24) Hanson, J. C.; Si, R.; Xu, W.; Senanayake, S. D.; Mudiyanselage, K.; Stacchiola, D.; Rodriguez, J. A.; Zhao, H.; Beyer, K. A.; Jennings, G.; et al. Pulsed-Reactant in Situ Studies of Ceria/CuO Catalysts Using Simultaneous XRD, PDF and DRIFTS Measurements. *Catal. Today* **2014**, *229*, 64−71.
(25) Gao, F.; Kwak, J. H.; Szanyi, J.; Peden, C. H. F. Current Understanding of Cu-Exchanged Chabazite Molecular Sieves for Use as Commercial Diesel Engine DeNO$_x$ Catalysts. *Top. Catal.* **2013**, *56*, 1441−1459.
(26) Hara, M.; Kondo, T.; Komoda, M.; Ikeda, S.; Kondo, J. N.; Domen, K.; Hara, M.; Shinohara, K.; Tanaka, A. Cu_2O as a Photocatalyst for Overall Water Splitting Under Visible Light Irradiation. *Chem. Commun.* **1998**, 357−358.
(27) Sträter, H.; Fedderwitz, H.; Groß, B.; Nilius, N. Growth and Surface Properties of Cuprous Oxide Films on Au(111). *J. Phys. Chem. C* **2015**, *119*, 5975−5981.
(28) Yin, M.; Wu, C.-K.; Lou, Y.; Burda, C.; Koberstein, J. T.; Zhu, Y.; O'Brien, S. Copper Oxide Nanocrystals. *J. Am. Chem. Soc.* **2005**, *127*, 9506−9511.
(29) Bendavid, L. I.; Carter, E. A. First-Principles Predictions of the Structure, Stability, and Photocatalytic Potential of Cu_2O Surfaces. *J. Phys. Chem. B* **2013**, *117*, 15750−15760.
(30) Besenbacher, F.; Nørskov, J. K. Oxygen Chemisorption on Metal Surfaces: General Trends for Cu, Ni and Ag. *Prog. Surf. Sci.* **1993**, *44*, 5−66.
(31) Gattinoni, C.; Michaelides, A. Atomistic Details of Oxide Surfaces and Surface Oxidation: The Example of Copper and Its Oxides. *Surf. Sci. Rep.* **2015**, *70*, 424−447.
(32) Sueyoshi, T.; Sasaki, T.; Iwasawa, Y. Molecular and Atomic Adsorption States of Oxygen on Cu(111) at 100−300 K. *Surf. Sci.* **1996**, *365*, 310−318.
(33) Xu, Y.; Mavrikakis, M. Adsorption and Dissociation of O_2 on Cu(111): Thermochemistry, Reaction Barrier and the Effect of Strain. *Surf. Sci.* **2001**, *494*, 131−144.
(34) Wiame, F.; Maurice, V.; Marcus, P. Initial Stages of Oxidation of Cu(111). *Surf. Sci.* **2007**, *601*, 1193−1204.
(35) Lawton, T. J.; Pushkarev, V.; Broitman, E.; Reinicker, A.; Sykes, E. C. H.; Gellman, A. J. Initial Oxidation of Cu(hkl) Surfaces Vicinal to Cu(111): A High- Throughput Study of Structure Sensitivity. *J. Phys. Chem. C* **2012**, *116*, 16054−16062.
(36) Pérez León, C.; Sürgers, C.; Löhneysen, H. v. Formation of Copper Oxide Surface Structures via Pulse Injection of Air onto

DOI: 10.1021/acs.jpcc.6b01284
J. Phys. Chem. C 2016, 120, 10879−10886

Cu(111) Surfaces. *Phys. Rev. B: Condens. Matter Mater. Phys.* **2012**, *85*, 035434.
(37) Matsumoto, T.; Bennett, R. A.; Stone, P.; Yamada, T.; Domen, K.; Bowker, M. Scanning Tunneling Microscopy Studies of Oxygen Adsorption on Cu(111). *Surf. Sci.* **2001**, *471*, 225−245.
(38) Yang, F.; Choi, Y.; Liu, P.; Stacchiola, D.; Hrbek, J.; Rodriguez, J. A. Identification of 5−7 Defects in a Copper Oxide Surface. *J. Am. Chem. Soc.* **2011**, *133*, 11474−11477.
(39) Kronawitter, C. X.; Riplinger, C.; He, X.; Zahl, P.; Carter, E. A.; Sutter, P.; Koel, B. E. Hydrogen-Bonded Cyclic Water Clusters Nucleated on an Oxide Surface. *J. Am. Chem. Soc.* **2014**, *136*, 13283−13288.
(40) Jensen, F.; Besenbacher, F.; Lægsgaard, E.; Stensgaard, I. Oxidation of Cu(111): Two New Oxygen Induced Reconstructions. *Surf. Sci.* **1991**, *259*, L774−L780.
(41) Jensen, F.; Besenbacher, F.; Stensgaard, I. Two New Oxygen Induced Reconstructions on Cu(111). *Surf. Sci.* **1992**, *270*, 400−404.
(42) Noh, J.; Zong, K.; Park, J. B. Molecular-Scale Investigation of Reconstructed Copper Surface Induced by Dissociative Adsorption of O_2. *Bull. Korean Chem. Soc.* **2011**, *32*, 1129−1130.
(43) Judd, R. W.; Hollins, P.; Pritchard, J. The Interaction of Oxygen with Cu(111): Adsorption, Incorporation and Reconstruction. *Surf. Sci.* **1986**, *171*, 643−653.
(44) Moritani, K.; Okada, M.; Sato, S.; Goto, S.; Kasai, T.; Yoshigoe, A.; Teraoka, Y. Photoemission Study of the Translational Energy Induced Oxidation Processes on Cu(111). *J. Vac. Sci. Technol., A* **2004**, *22*, 1625−1630.
(45) Moritani, K.; Okada, M.; Sato, S.; Goto, S.; Kasai, T.; Yoshigoe, A.; Teraoka, Y. Translational Energy Induced Reconstruction and Absorption in the Oxidation Processes of Cu{111}. *Thin Solid Films* **2004**, *464−465*, 48−51.
(46) Moritani, K.; Okada, M.; Teraoka, Y.; Yoshigoe, A.; Kasai, T. Reconstruction of Cu(111) Induced by a Hyperthermal Oxygen Molecular Beam. *J. Phys. Chem. C* **2008**, *112*, 8662−8667.
(47) Dubois, L. H. Oxygen Chemisorption and Cuprous Oxide Formation on Cu(111): A High Resolution EELS Study. *Surf. Sci.* **1982**, *119*, 399−410.
(48) An, W.; Baber, A. E.; Xu, F.; Soldemo, M.; Weissenrieder, J.; Stacchiola, D.; Liu, P. Mechanistic Study of CO Titration on Cu_xO/Cu(111) ($x \leq 2$) Surfaces. *ChemCatChem* **2014**, *6*, 2364−2372.
(49) Mudiyanselage, K.; An, W.; Yang, F.; Liu, P.; Stacchiola, D. J. Selective Molecular Adsorption in Sub-Nanometer Cages of a Cu_2O Surface Oxide. *Phys. Chem. Chem. Phys.* **2013**, *15*, 10726−10731.
(50) Richter, N. A.; Kim, C.-E.; Stampfl, C.; Soon, A. Re-Visiting the O/Cu(111) System − When Metastable Surface Oxides Could Become an Issue! *Phys. Chem. Chem. Phys.* **2014**, *16*, 26735−26740.
(51) Önsten, A.; Göthelid, M.; Karlsson, U. O. Atomic Structure of Cu_2O(111). *Surf. Sci.* **2009**, *603*, 257−264.
(52) Johnston, S. M.; Mulligan, A.; Dhanak, V.; Kadodwala, M. The Structure of Disordered Chemisorbed Oxygen on Cu(111). *Surf. Sci.* **2002**, *519*, 57−63.
(53) An, W.; Xu, F.; Stacchiola, D.; Liu, P. Potassium-Induced Effect on the Structure and Chemical Activity of the Cu_xO/Cu(111) ($x \leq 2$) Surface: A Combined Scanning Tunneling Microscopy and Density Functional Theory Study. *ChemCatChem* **2015**, *7*, 3865−3872.
(54) Soon, A.; Todorova, M.; Delley, B.; Stampfl, C. Thermodynamic Stability and Structure of Copper Oxide Surfaces: A First-Principles Investigation. *Phys. Rev. B: Condens. Matter Mater. Phys.* **2007**, *75*, 125420.
(55) Soon, A.; Todorova, M.; Delley, B.; Stampfl, C. Oxygen Adsorption and Stability of Surface Oxides on Cu(111): A First-Principles Investigation. *Phys. Rev. B: Condens. Matter Mater. Phys.* **2006**, *73*, 165424.
(56) Soon, A.; Todorova, M.; Delley, B.; Stampfl, C. Surface Oxides of the Oxygen-Copper System: Precursors to the Bulk Oxide Phase? *Surf. Sci.* **2007**, *601*, 5809−5813.
(57) Kresse, G.; Hafner, J. Ab Initio Molecuar Dynamics for Liquid Metals. *Phys. Rev. B: Condens. Matter Mater. Phys.* **1993**, *47*, 558−561.
(58) Kresse, G.; Furthmuller, J. Efficient Iterative Schemes for Ab Initio Total-Energy Calculations Using a Plane-Wave Basis Set. *Phys. Rev. B: Condens. Matter Mater. Phys.* **1996**, *54*, 11169−11186.
(59) Blochl, P. E. Projector Augmented-Wave Method. *Phys. Rev. B: Condens. Matter Mater. Phys.* **1994**, *50*, 17953−17979.
(60) Kresse, G.; Joubert, D. From Ultrasoft Pseudopotentials to the Projector Augmented-Wave Method. *Phys. Rev. B: Condens. Matter Mater. Phys.* **1999**, *59*, 1758−1775.
(61) Perdew, J. P.; Burke, K.; Ernzerhof, M. Generalized Gradient Approximation Made Simple. *Phys. Rev. Lett.* **1996**, *77*, 3865−3868.
(62) *CRC Handbook of Chemistry and Physics*; CRC Press: New York, 2002.
(63) Tersoff, J.; Hamann, D. R. Theory and Application for the Scanning Tunneling Microscope. *Phys. Rev. Lett.* **1983**, *50*, 1998−2001.
(64) Tersoff, J.; Hamann, D. R. Theory of the Scanning Tunneling Microscope. *Phys. Rev. B: Condens. Matter Mater. Phys.* **1985**, *31*, 805−813.

DOI: 10.1021/acs.jpcc.6b01284
J. Phys. Chem. C 2016, 120, 10879−10886